

Lift force coefficient of ellipsoidal single bubbles in water

H. Hessenkemper^{a,*}, T. Ziegenhein^{a,b}, R. Rzehak^a, D. Lucas^a, A. Tomiyama^c

^a Helmholtz-Zentrum Dresden-Rossendorf, Institute of Fluid Dynamics, Bautzner Landstraße 400, 01328 Dresden, Germany

^b School for Engineering of Matter, Transport and Energy, Arizona State University, Tempe, AZ 85287, USA

^c Graduate School of Engineering, Kobe University, 1-1, Rokkodai, Nada, Kobe 657-8501, Japan



ARTICLE INFO

Article history:

Received 8 April 2020

Revised 4 January 2021

Accepted 2 February 2021

Available online 4 February 2021

Keywords:

Lift coefficient

Bubbly flows

Turbulent flow

Impurities

ABSTRACT

For the simulation of bubbly flows, knowledge of the lift force as an interaction between gas bubbles and a surrounding shear field is of great importance. The sign of the lift coefficient C_L changes with increasing bubble size, i.e. with more pronounced bubble deformation. Beside this, impurities in terms of surface-active components are well-known to change the complete hydrodynamic behavior of a bubble even if the amount is very small. In the present work, the lift coefficient of single ellipsoidal bubbles is determined with a recently developed method, which is suitable to overcome difficulties connected to low viscous systems. In order to investigate the influence of impurities on the lift force, we conducted experiments with single bubbles of different sizes in purified, deionized and tap water. Overall, the determined lift coefficients show no difference between deionized and tap water but reveal differences to results obtained with purified water. As no significant differences in shape and velocity are found between the different water qualities, it remains unclear how the impurities cause the observed differences. For the deionized and tap water results that are more relevant in practice, a new correlation is proposed to account for the observed differences in comparison to data from the literature. It can be used to calculate C_L of ellipsoidal bubbles in the investigated size range.

© 2021 Elsevier Ltd. All rights reserved.

1. Introduction

Bubbly flows occur in many industrial applications, e.g. in chemical engineering, bioreactors or power plants. The knowledge of characteristic parameters like gas volume fraction and bubble size distributions are of great importance for the design of corresponding facilities, the optimization of processes and for a safe operation. The spatial distribution of bubbles is influenced by the momentum exchange between the continuous liquid phase and the dispersed bubbles. The bubble drag is often stated as the most important interaction force since it determines the momentum exchange due to the slip velocity between both phases (Sokolichin et al., 2004). However, also the lift force has a major influence on the lateral void distribution in bubbly flows (Besagni and Inzoli, 2016; Lopez de Bertodano et al., 1994) and is supposed to stabilize or destabilize a flow regime depending on its sign (Lucas et al., 2005). Recently, Muniz and Sommerfeld (2020) have performed a detailed numerical analysis of relevant bubble forces in bubble column and underlined the im-

tance of the lift force with respect to the correct prediction of void distributions.

Correlations available in the literature to calculate the lift force are often restricted to specific parameter ranges like high viscous liquids (Tomiyama et al., 2002b) or small bubble Reynolds numbers (Legendre and Magnaudet, 1998). An adoption to other systems is not always possible as demonstrated by Aoyama et al. (2017). Especially, the lift force acting on bubbles in a broad range of industrial cases, i.e. low viscous liquids like water, has not been investigated satisfactory so far and is a main subject of the present work.

In general, the lift force acting on small, spherical bubbles that pass a shear field is different from that acting on larger, ellipsoidal bubbles. Spherical bubbles are pushed into the direction of decreasing liquid velocity and form a wall-peak void distribution in a co-current upward flow. This is accounted for with a positive lift coefficient C_L in the definition of the lift force given by Žun (1980):

$$\vec{F}_{Lift} = C_L \rho_L (\vec{u}_G - \vec{u}_L) \times \text{rot}(\vec{u}_L), \quad (1)$$

where the subscripts G and L denote the gas and liquid phases, ρ the density and \vec{u} the velocity. For this lift force formulation, Žun (1980) reported C_L values of about 0.3 for bubbles smaller than 2 mm spherical equivalent diameter, which were suspended in a tap water stream. Auton (1987) derived a lift coefficient of 0.5 for

* Corresponding author.

E-mail address: h.hessenkemper@hzdr.de (H. Hessenkemper).

a clean spherical bubble of high Reynolds number ($Re \geq 50$), both numerically and analytically. A quite similar behavior was reported by Legendre and Magnaudet (1998), who conducted simulations of a clean spherical bubble in a linear shear flow. For higher bubble Reynolds numbers up to 500, C_L asymptotically approaches also a value of 0.5 in their work.

With increasing bubble Reynolds number, the bubble shape changes from spherical to ellipsoidal. As reported by numerous studies in the literature, the lift coefficient changes from a positive value to a negative value for bubbles with a distinct deformation (Bothe et al., 2006; Ervin and Tryggvason, 1997; Kariyasaki, 1987; Lucas and Tomiyama, 2011). Consequently, such bubbles move in the direction of increasing liquid velocity and form core-peaked void distributions in a classical upward pipe flow or bubble column. A widely used correlation for this sign change was proposed by Tomiyama et al. (2002), who determined experimentally the lift coefficient for single bubbles of different sizes in high viscous liquids. Their correlation is based on the major axis of a bubble to account for the bubble deformation, which is stated to be responsible for this changed lift force behavior. Tomiyama et al. (1995) conducted simulations of single bubbles in a Poiseuille flow and connected the sign change to a slanted wake behind the bubble, which is caused by a wake-shear field interaction. Adoua et al. (2009) also investigated the C_L behavior of oblate spheroidal bubbles numerically and its connection to the bubble shape. They pointed out that the interaction of the shear field and the vorticity generated at the bubble surface is responsible for the sign change, whereby the latter is again dependent on the bubble deformation and the mobility of the bubble surface (Fan and Tsuchiya, 1990).

To bring further insight to the lift force behavior in dilute systems, which are mostly characterized by a turbulent liquid flow and higher bubble Reynolds numbers, the lift coefficient of single bubbles rising in water are investigated in the present work. The work bases on a new measuring method developed by Ziegenhein et al. (2018). Their preliminary results for the lift coefficient still showed a rather large scattering, but already improved the results in the work of Muniz and Sommerfeld (2020) in comparison to the usually used Tomiyama correlation. In our recent work we refined the procedure to reach higher reproducibility and started to analyze contamination effects by adding sodium chloride as an inorganic surfactant to our system (Hessenkemper et al., 2020). Although we were able to reveal an effect on smaller bubbles, the question on the role of unknown contaminations like organic surfactants present as impurities in the liquid phase arose, since only deionized water and not purified water was used as an uncontaminated reference. In the present work we are addressing this issue by comparing results obtained with different water qualities, namely deionized, tap and purified water.

2. Experimental setup and measuring method

2.1. Facility and method

The experimental facility consists of a rectangular bubble column made of Plexiglas, which is schematically depicted in Fig. 1. The column is filled with deionized water (DI), tap water or purified water to a fill height of 900 mm at the beginning of each experiment. The purified water is obtained by a Milli-Q Gradient A10 water purification system.

In the past, often a rotating belt, which can be interpreted as a moving wall, was used to generate a linear velocity gradient in the liquid phase (Aoyama et al., 2017; Tomiyama et al., 2002b). This technique is, however, only suitable for higher viscous liquids, since it does not provide a strong enough and linear gradient in low viscous liquids like water. The concept of Ziegenhein et al. (2018) is to use a volumetric force instead of a

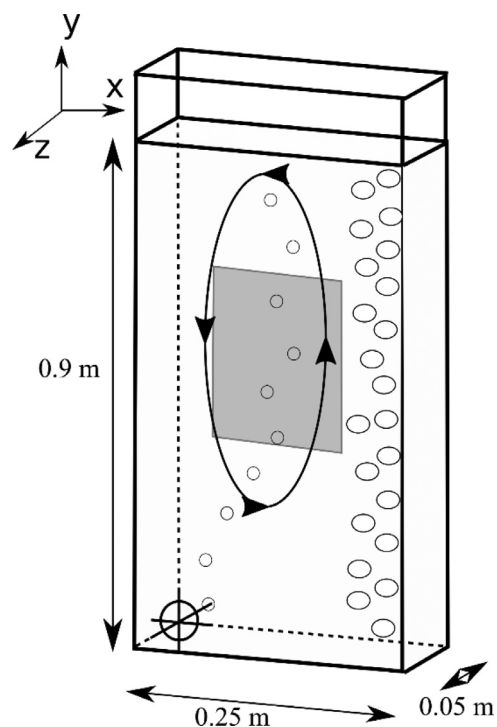


Fig. 1. Sketch of the bubble column with indication of liquid flow direction. Gray region indicates field of view.

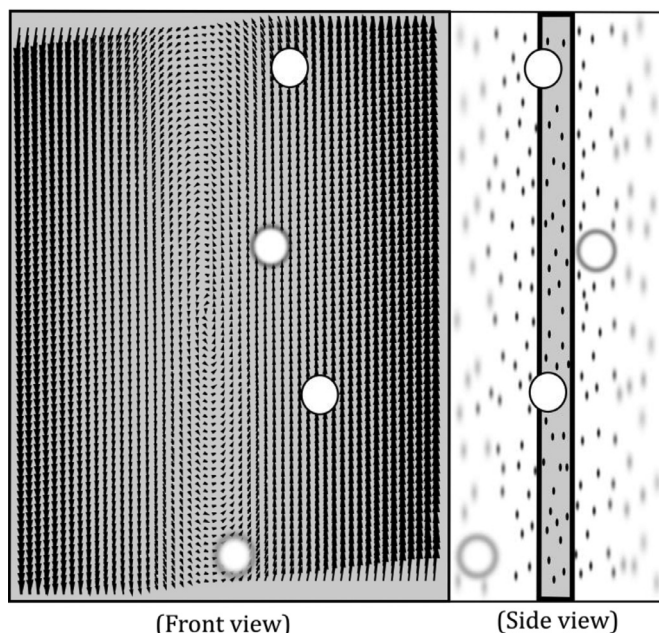


Fig. 2. Schematic representation of the PSV method as it is applied in the current work. Left: Field of view with an exemplary average liquid velocity field and passing single bubbles as seen from the column front. Right: Representation of the sharpness region in the column center as seen from the column side.

wall force to accelerate the liquid. This force is provided with a bubbly flow generated at the column side, which induces an elongated vortex in the upper section of the column as indicated by the arrows in Fig. 1. Four 0.6 mm spargers generate this bubbly flow with a constant flowrate of 0.8 l/min. Although the flow is moderately turbulent, the vertical velocity component of a time-averaged vortex has a linear gradient. An exemplary time-averaged

liquid velocity field of such a vortex is given in Fig. 2 on the left side.

A single sparger continuously generates single bubbles at the opposite positions of the column bottom. These single bubbles rise through the shear field of the generated vortex, where they are analyzed with respect to their lift force behavior via a force balance. With the use of various sparger sizes, single bubbles in the range of 2.2–6.5 mm spherical equivalent diameter are generated with flowrates up to max. 15 ml/min. Such small flowrates ensure that ascending single bubbles have a sufficient distance of about 10 cm to each other.

In order to evaluate the force balance of oscillating bubbles rising through a turbulent background flow, a suitable averaging procedure is necessary. This averaging procedure is briefly described in the following.

As a first step of the averaging procedure, a rectangular 2D grid with a cell size of 0.5 mm is defined, which has the dimensions of the field of view (cf. Fig. 1). The measured bubbles are transferred to this grid so that a gas volume fraction distribution can be calculated, where only bubbles with a sufficient distance to the column wall are considered. With this distribution, an average bubble rise path is calculated using the gas fraction maxima along the height. Afterwards, this discrete rise path is smoothed with a spline interpolation and the corresponding average liquid velocities are interpolated by fourth order to the local path coordinates. Since the path is in the column center, the symmetrical wall forces can be neglected. Therefore, the lift force can be calculated by the following force balance:

$$\bar{F}_{\text{Lift}} = \bar{F}_{\text{Buoyancy}} + \bar{F}_{\text{Drag}} + \bar{F}_{\text{VirtualMass}}. \quad (2)$$

Substituted with the corresponding force terms the force balance reads:

$$-\bar{C}_L \rho_L (\bar{u}_G - \bar{u}_L) \times \text{rot}(\bar{u}_L) = \Delta \rho \vec{g} + \frac{3}{4} \frac{1}{d_B} C_D \rho_L |\bar{u}_G - \bar{u}_L| (\bar{u}_G - \bar{u}_L) + C_{VM} \rho_L \frac{D\bar{u}_L}{Dt}. \quad (3)$$

Here, d_B denotes the sphere-volume equivalent diameter. The bar over the values represents a time-averaged value, which is omitted in the following for a better clarity. The drag coefficient C_D is calculated with a vertical force balance, whereby the vertical lift force is assumed negligible. Although the virtual mass force has only a minor influence on the obtained lift coefficient due to the time-averaged consideration, it is still retained in the calculation. The virtual mass coefficient C_{VM} is calculated as proposed by Lamb (1932) and takes values between 0.55 and 1.15. A detailed derivation of equation (3) as well as further discussions on the made assumptions can be found in Ziegenhein et al. (2018).

To compare the gained lift coefficient with data from the literature, the Eötvös number as well as the modified Eötvös number Eo_{\perp} are used

$$Eo = \frac{\Delta \rho g d_B^2}{\sigma}, \quad Eo_{\perp} = \frac{\Delta \rho g d_{Major}^2}{\sigma}, \quad (4)$$

where d_{Major} denotes the major axis of the bubble.

2.2. Measurement technique

To calculate the lift force with the procedure described above, the liquid velocity and the bubble movement have to be measured. In the work by Ziegenhein et al. (2018), this was done separately. The liquid velocity was measured with conventional PIV using a laser sheet, while the bubbles were recorded with stereoscopic shadowgraphy in a second step. However, this could introduce a position error due to slight misalignments as discussed in their work. In our recent work Hessenkemper et al. (2020), we

introduced simultaneous measurements of the necessary quantities for both phases, which completely avoids such errors. This is achieved by the use of a small depth of field (DOF) and adapted shadowgraphy techniques, as it was applied by Bröder and Sommerfeld (2007). This technique adopted in the present setup is depicted in Fig. 2.

As shown in Fig. 2 on the side view of the column, the use of a small DOF results in a thin sharpness region (grayed out in the figure). The projections of objects inside this region are captured with sharp edges, while with increasing distance to this region these edges are more and more blurred. When tracer particles are added to the flow (black dots in the figure), the liquid velocity can be determined in a quasi-2D region with suitable post-processing procedures.

The determination of liquid velocity fields with this sharpness technique is commonly referred as Particle Shadow Velocimetry (PSV) in the literature (Estevadeordal and Goss, 2005). For this, the flow is seeded with 100 μm neutrally buoyant Polyamid Seeding Particles in the present work. This comparably large tracer size is needed to obtain a sufficient large particle shadow in the images, but may not completely follow the relevant fluctuating time and length scales. By taking into account the added mass (Calzavarini et al., 2008), the characteristic particle time scale can be estimated to about 0.83 ms. Although this is two to three times longer than commonly used seeding particles in bubbly flows, Ziegenhein et al. (2016) have shown that characteristic time scales of 2.5 ms are still able to capture the relevant fluid fluctuations. Furthermore, we demonstrated in Hessenkemper et al. (2020) that the used particle concentration is small enough not to additionally contaminate the bubbles.

The post-processing is done with an in-house made procedure called Particle Shadow Image Velocimetry (PSIV), which is described in Hessenkemper and Ziegenhein (2018). This procedure uses standard cross-correlation methods as it is usually done in PIV post-processing steps. Moreover, the PSIV procedure provides a bubble mask to exclude bubble shadows in the correlation step as well as the so-called particle sharpening step. The latter can be used to manipulate the effective DOF, which is also called the depth of correlation in PSV measurements. This is done via pronouncing sharp particles in comparison to blurred particles before the velocity determination.

Besides the liquid velocity, the properties of the gas bubbles have to be determined from the recorded images. The used sharpness technique grants another advantage, since it allows us to distinguish sharp bubbles in the column center from blurred bubbles closer to the wall region without stereoscopic measurements. The elimination of bubbles closer to the wall is important for two reasons. First, gradients of the vertical liquid velocity in direction of the z-coordinate (cf. Fig. 1) appear in these wall regions as it was shown by Ziegenhein et al. (2018). Since such depth gradients are neglected in the calculation, this could bias the results. Second, additional wall effects like the neglected wall force could have an influence on the bubble movement and therefore on the lift force measurement.

The algorithm used for the bubble identification is based on the Sobel operator, which calculates the pixel gray value derivatives along the edges of an object. Edges with strong derivatives are selected via a threshold so that only sharp bubbles in the center region are included. From these validated edges, the bubbles are then reconstructed and necessary properties are extracted. Important geometric properties are the bubble size as well as the bubble shape. For the size, the sphere-volume equivalent diameter d_B is determined using the solid of revolution of the projected bubble. The shape is represented via the aspect ratio as the ratio of the bubble minor axis to the bubble major axis. In this context, the major axis d_{Major} is defined as the largest extent of the bubble

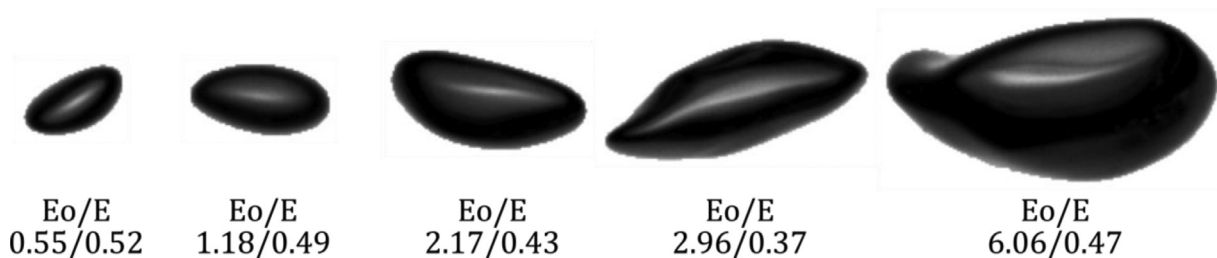


Fig. 3. Exemplary bubble images with calculated Eötvös number E_o and aspect ratio E .

projection and the minor axis d_{Minor} as the largest extent perpendicular to the major axis (Ziegenhein and Lucas, 2017). Since the bubble geometry is reconstructed only from the 2D-front view of the column (cf. Fig. 2), perspective errors of the bubble size and shape due to wobbling surfaces and tilted bubble orientations are inevitable. From pretests we could estimate a bubble size error below 5 % for the average bubble diameter. However, Bröder and Sommerfeld, (2007) showed that in dependence of the bubble orientation this error can take much higher values for a 2 mm bubble. Furthermore, it is likely that this error may depend on the bubble size and the correspondingly changed strength of the bubble surface oscillation, so that more detailed studies are needed to obtain accurate error estimates of the bubble size. The error of the bubble shape was not accessible, but may take larger values. In addition to the bubble geometries, the bubble velocity is determined via tracking the centroid of the projected bubble area. Exemplary bubble images with calculated size and shape are given in Fig. 3.

The DOF in the present work is adjusted and calibrated to a thickness of about 1 cm. For calibrating the DOF, a flat target is positioned in the column center and sample images with the same settings as in the experiments are taken. The camera is moved stepwise with a linear unit and the target pixel derivatives are calculated from the recorded images. With this procedure, the corresponding thresholds for the particle sharpening is adjusted to the same distance as the DOF of ± 5 mm from the center of sharpness. For the bubble identification, a threshold with a distance of ± 1 cm and therefore double the distance as for the particle sharpening is chosen. With this distance sufficient bubbles can be evaluated, which are assumed to be still far enough away from the problematic wall region. An example with simultaneously determined liquid velocities as well as gas bubbles is given in Fig. 4. The bubble in the lower right corner is inside the sharpness region, while the bubble at the top left is outside and therefore not in the column center region.

For determining the required quantities, the flow is recorded with an IDS UI-3160CP camera and a 135 mm f2.0 Walimex Pro foto lens. Pairs of double images are recorded with a framerate of 180 fps and a delay of 75 ms is set before the next image pair is recorded. The images have a resolution of 1920×1200 pixels, resulting in a pixel size of $53 \mu\text{m}$ and are continuously streamed to a PC. Thus, a more than four times higher resolution in comparison to the previous experiments is used in order to increase the accuracy of the measurements. A measurement time of 90 mins is chosen for each experiment, resulting in approximately 60 000 image pairs and therefore 60 000 liquid velocity fields as well as 30 000–140 000 validated sharp single bubbles. This high amount of data is necessary to calculate a stable average rise path due to the mentioned difficulties of a turbulent flow field and oscillating bubble motions. Discussion on the necessity of such a large sample size follows in section 4.2. Since no laser sheet is required for the described PSV method, the whole setup is backlight illuminated with a 200 W LED lamp only. To gain a homogenous illumination of the field of view, a diffusor plate is placed between the

lamp and the column. All experiments are conducted under ambient pressure and room temperature between 20–22°C.

3. Evaluation of the water quality

3.1. Determination of impurity related system properties

In order to estimate the amount of relevant impurities in the water, various properties of the liquid phase and the liquid-gas interface can be measured. Relevant are in this context substances that change the surface tension and are hence able to induce contamination effects like the well-known Marangoni-effect on bubbles (Cuenot et al., 1997). Hereby, the total organic carbon (TOC) value, which also includes most of surfactants, the electrical resistivity or electrical conductivity for ionic components as well as the surface tension are used. For the purified water, the Milli-Q purification system monitors the TOC value as well as the electrical resistivity during the extraction of the water. For the DI and tap water, the electrical conductivity is monitored during the extraction and the TOC value of corresponding samples were analyzed in an external laboratory. Furthermore, the surface tension was measured with a bubble pressure tensiometer that allows a dynamic determination of the surface tension. Hence, transient changes due to the adsorption of small amounts of surfactants can be captured. All of the gathered values are summarized in Table 1.

As can be seen in Table 1 the TOC value differs for all three types of water. Unfortunately, the TOC value of DI-water is below the determination limit of the used method. It is assumed that the value is still larger than the TOC value of purified water. However, the TOC value does not contain information of the type of organic components, which could be also other organic materials than surfactants, so that a direct conclusion regarding the effect of remaining impurities on a bubble is not possible. The same trend is also observable for the electrical resistivity. Again, the values for DI-water and tap water are out of the measurement limit. Nevertheless, the difference is more than an order of magnitude. In contrast, the surface tension is the same for all three types of water even after a measuring time of 10 mins.

3.2. Pretests in quasi-stagnant liquid

Although the previous attempt to quantify the water quality gives a general impression on remaining impurities, a clear derivation of expectable changes of the bubble hydrodynamics is not possible. The values were measured separately, which means that the real value during an experiment might be different and since an open bubble column is used, airborne contaminations may enter the system during a measurement. It becomes even more complicated due to the fact that contamination effects depend on the bubble size. In order to further analyze and quantify the influence of the different purity levels on a bubble, experiments with single bubbles rising in a quasi-stagnant liquid are carried out. Hereby, the bubble rise behavior, e.g. terminal velocity or bubble shape, can

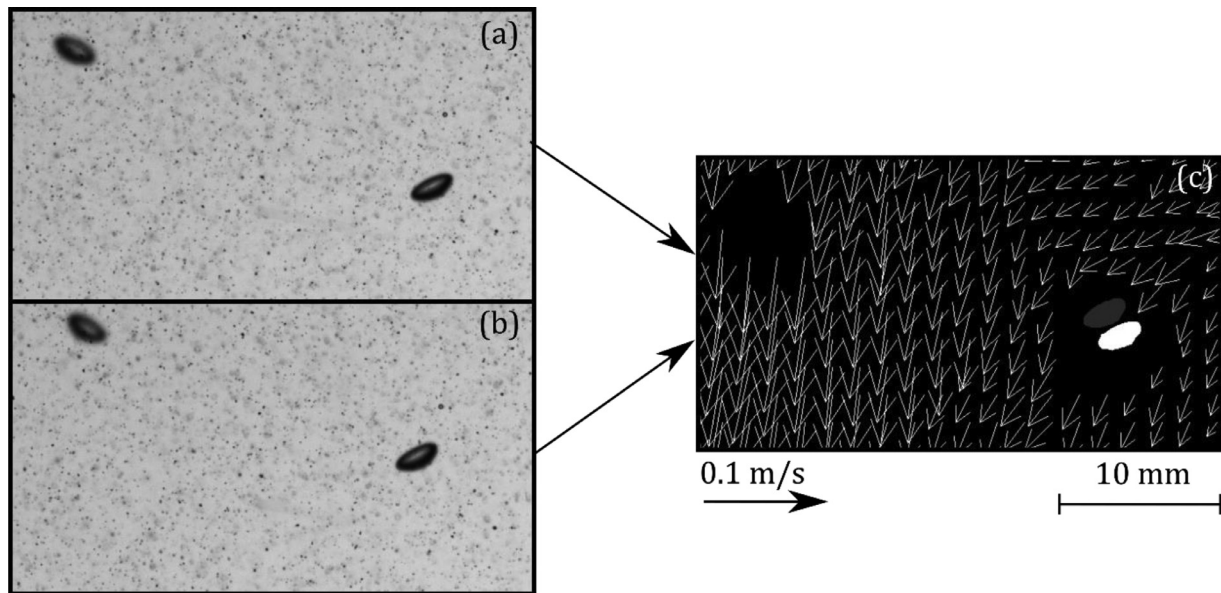


Fig. 4. (a+b) Exemplary image pair with a sharp and a blurred bubble as well as added tracer particles; (c) Resulting liquid velocity and reconstructed, sharp bubbles (all images are cropped for reasons of space).

Table 1
Properties of the used waters regarding impurities.

Type of water	TOC [ppm]	Electrical resistivity [MΩcm]	Surface tension [N/m]
Tap water	1.3	< 0.5	0.0726
DI-water	< 0.5	> 1.0	0.0723
Purified water	$1\text{--}2 \cdot 10^{-3}$	18.2–18.3	0.0727

be compared to data from the literature. This is a common way to prove the purity of the used water, since accurate values obtained in ultra-purified water are available in the literature, at least up to a bubble size of 2.0 mm (Duineveld, 1995; Tagawa et al., 2014).

Three different bubble sizes in the range of 2.0 – 3.5 mm are investigated as these small bubbles are expected to be most sensitive to impurities. The bubbles are measured at a measuring height of 0.75 m to allow an adsorption of surfactants that might be present in very small concentrations. In order to correctly determine the bubble velocity, the bubbles are recorded stereoscopically in these pretests.

The first indicator for impurities that is examined is the terminal velocity of a bubble. As in the lift force experiments, bubbles are released continuously to measure a large number of bubbles in a relatively short time. Although this technique provides a sufficient large sample size to calculate accurate mean values, the continuous bubble generation can generate a slow but not negligible background flow in the column even if the generation frequency is rather small (~1 Hz). If this is the case, the liquid cannot be regarded as quiescent anymore and the terminal velocity is better approximated with the slip velocity $u_{\text{Slip}} = u_{\text{Bubble}} - u_{\text{Liquid}}$.

The average slip velocity results are shown in Fig. 5(a). Generally, the results are in good agreement to the DNS-based correlation by Dijkhuizen et al. (2010a), which proves an overall good water quality of all three types of water. For the smallest bubble size, the results are very close to the results by Duineveld (1995), who determined bubble velocities in ultra-purified water. However, the results for purified water are slightly closer to this reference than the two others. This indicates that although the amount of impurities is rather small in the tap and DI-water, it might be even smaller in the purified water. For the latter, the remaining difference might be caused by the slightly larger bubble size of 2.02 mm in comparison to 1.94 mm in the reference of Duineveld (1995).

The differences between the three tested water qualities is only minor for the second bubble size and non-existent for the third bubble size. In that case, the influence of impurities on the velocity is negligible.

As another indicator for impurities, the bubble shape is additionally analyzed. Fig. 5(b) shows the aspect ratio in comparison to literature data. Clearly, the results obtained in purified water show the smallest aspect ratios and therefore the largest deformation, which is even slightly smaller than the result of Duineveld (1995). Again, the slightly different bubble size might be the reason for this. The results obtained in tap and DI-water show higher aspect ratios for the two smallest bubble sizes. Note that the aspect ratio scale is rather small. Only for the largest bubble size of this pretest the results coincide again, where a good agreement to the data of Veldhuis et al. (2008) for this bubble size can be seen.

From these pretests it seems that impurities in the three waters only play a role on bubbles smaller than at least 3 mm. Although the experimental setup is an open system and contaminations may enter the system during an experiment, their influence is negligible in the purified water case as the velocity and shape results are in good agreement with literature data for ultra-purified water. The DI-water and tap water results show small deviations to the literature reference and seem to contain a somewhat higher amount of impurities.

4. Lift force experiments

4.1. Liquid vortex

The liquid vortex is a crucial part of the used method, since it provides the required linear shear field. To examine the reproducibility of the vortex, three different profiles for the average vertical liquid velocity are depicted in Fig. 6(a). These measurements

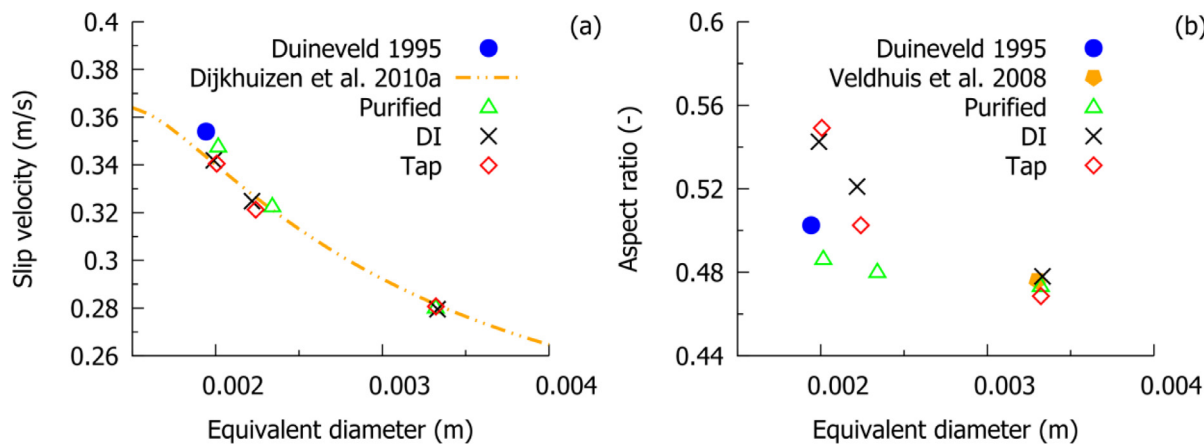


Fig. 5. Influence of impurities on the bubble velocity and shape. Results of the average (a) slip velocity and (b) aspect ratio.

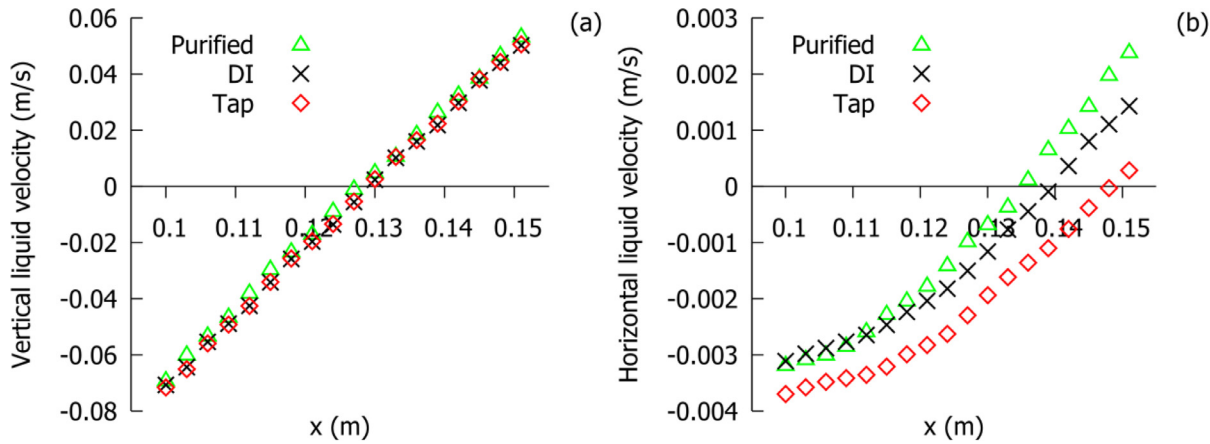


Fig. 6. Velocity profiles of the (a) vertical and (b) horizontal liquid velocity.

are done with a running driving bubbly flow at the column side plus the injected single bubbles to include possible effects of the rising single bubbles on the flow field for which the different water types are used. As can be seen, all three profiles overlap each other and a linear shear field is granted from a time-average point of view. Additionally, the average shear rate is the same for these experiments, which did also not differ for other single bubble sizes. Hence, the lift force is evaluated with an average shear rate of about $2.2\text{--}2.4 \text{ s}^{-1}$ along the bubble path in all experiments.

The horizontal velocity is of major importance in the experiments since it determines the lateral bubble movement in combination with the lift force. Corresponding profiles of the horizontal velocity are shown in Fig. 6(b) for the same experiments as for the vertical velocity. Small differences are visible for the different examples, which are also present for the vertical component but not visible through the different magnitude. An explanation for these differences is a unique position of each generated vortex, which means that the position in the column can be slightly different for different experiments. This could be a consequence of the filling procedure of the column before each experiment as described in Hessenkemper et al. (2020). Since the horizontal velocity is taken into account for the lift force evaluation, it is mandatory to measure both phase properties simultaneously and associate the correct liquid velocity field to the average bubble rise path.

The turbulence grade of the vortex is low to moderate, where the turbulence intensity I defined as $I = \sqrt{0.5(u'u' + v'v')}/\sqrt{u_{L,x}^2 + u_{L,y}^2}$ takes values of about 1 % in the region of interest. Here u' denotes the horizontal fluctuation

component and v' the vertical fluctuation component. The vertical fluctuation component v' shows slightly higher values than the horizontal component u' , which is typical for buoyancy driven bubbly flows (Parekh and Rzebak, 2018).

4.2. Statistical accuracy

Besides the methodical description of the lift force evaluation method, Ziegenhein et al. (2018) also presented some preliminary results for ellipsoidal bubbles in water. However, the results for the lift coefficient still showed a rather large scattering. Although the authors devoted an extensive error analysis to find reasons for the large scatter, some questions regarding potential error sources and uncertainties were still open.

The evaluation of errors and uncertainties biasing the results is a complex procedure for the used method. These error sources can be generally summarized as follows: Positioning errors due to misalignments of separate measurements, measurement errors, the influence of impurities as well as statistical uncertainties. The first error source regarding misalignments of separate measurements is completely avoided in the present work due to the simultaneous measurements of both phases. The higher image resolution used in this work generally increases the accuracy and hence reduces measurements errors. The influence of impurities is a major focus of this work and will be dealt with later in this chapter. Hence, it remains the statistical aspect.

In order to test the statistical accuracy, the behavior of the local lift coefficient along the average rise path is regarded at first. If the sample size is large enough, the lift force should be resolved

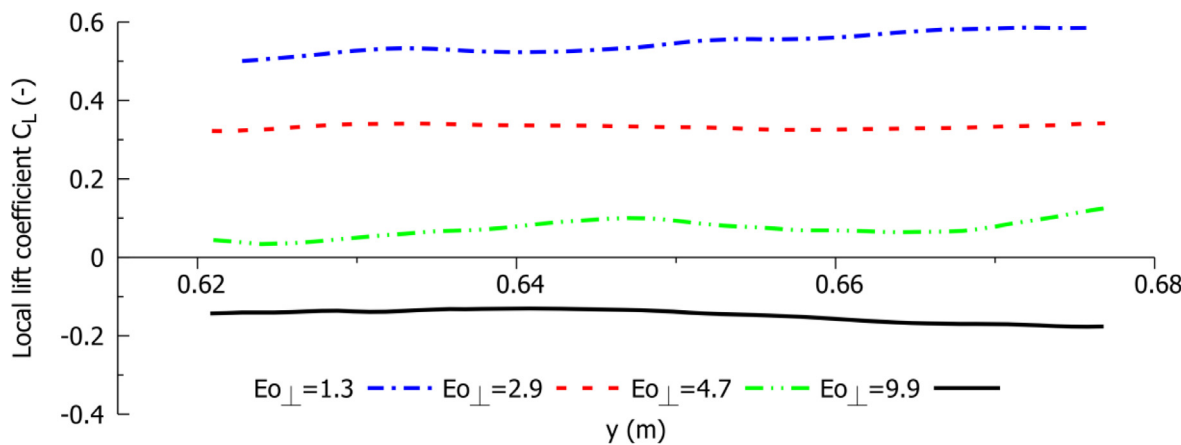


Fig. 7. Local lift coefficient along the average rise path for different bubble sizes.

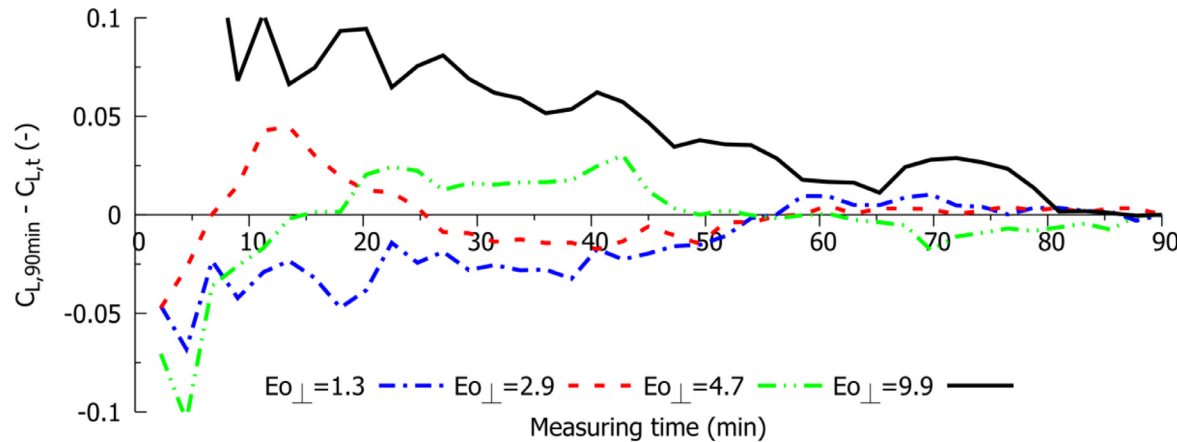


Fig. 8. Difference of $C_{L,t}$ calculated after specified measuring time to final $C_{L,90min}$ calculated after 90 min.

locally with the used averaging method and a constant lift coefficient along the path would be obtained. Fig. 7 demonstrates this behavior for four different bubble sizes in DI-water. The sample size for the shown cases is as follows: $Eo_{\perp} = 1.3 \rightarrow 73168$ bubbles, $Eo_{\perp} = 2.9 \rightarrow 114516$ bubbles, $Eo_{\perp} = 4.7 \rightarrow 72470$ bubbles, $Eo_{\perp} = 9.9 \rightarrow 33056$ bubbles. All four bubble sizes show an almost constant lift coefficient value with only small fluctuations along the path.

To further analyze the statistical accuracy, the difference of $C_{L,t}$ calculated after a specified measuring time to the final $C_{L,90min}$ calculated after 90 min is shown in Fig. 8. Here the C_L values are averaged along the path, which is also the case for all lift coefficient results in the following sections. As can be seen in Fig. 8, the calculated results do not change significantly anymore for the three smaller bubble sizes after around 50 min. This is a first demonstration of the increased reliability in comparison to the initial results by Ziegenhein et al. (2018). By accumulating the results of several individual measurements, they required a more than six times longer measurement time to achieve a similar convergence. In the present comparison, the largest bubble size shows slightly worse convergence behavior. To avoid any interaction of these larger bubbles, the generation frequency was reduced from about 1 Hz to 0.3 Hz so that also the amount of measured bubbles is smaller than for the other cases. Nevertheless, a longer measurement time and therefore a larger sample size is not expected to change the result significantly anymore, especially for the smaller bubble sizes. Hence, the remaining differences along the height in Fig. 7 have no

influence on the average lift coefficient results and the sample size can be considered as sufficient.

4.3. Bubble shape and velocity

Before the actual lift coefficient results are considered, first the velocity and shape results of all lift force experiments conducted are briefly discussed, similar to the previous pretests in quasi-stagnant liquid. Fig. 9 shows the vertical slip velocity for all investigated bubble sizes and types of water. For the smallest bubbles again the purified water case shows slightly larger values than the two other cases, whereby the results coincide for all other bubble sizes. The results from the lift force experiments are also consistent with the results of the pretest.

The bubble shape is shown in Fig. 10, where the major axis (a) and the aspect ratio (b) are given separately. The major axis results are compared to the correlation proposed by Wellek et al. (1966), which can be formulated as follows:

$$d_{Major} = d_B 3 \sqrt{1 + A Eo^B} \quad (5)$$

The coefficients $A=0.163$, $B=0.757$ proposed by Wellek et al. (1966) underestimate the bubble major axis in comparison to the results of this work, since they are valid only for contaminated systems (Okawa et al., 2003; Tomiyama et al., 2002a). Okawa et al., 2003 proposed the coefficients $A=1.97$, $B=1.3$ for pure systems. Although the measured major axis strongly deviates for larger bubbles sizes, good agreement is obtained for small bubbles with $Eo < 1$. This is most probably due to the fact, that

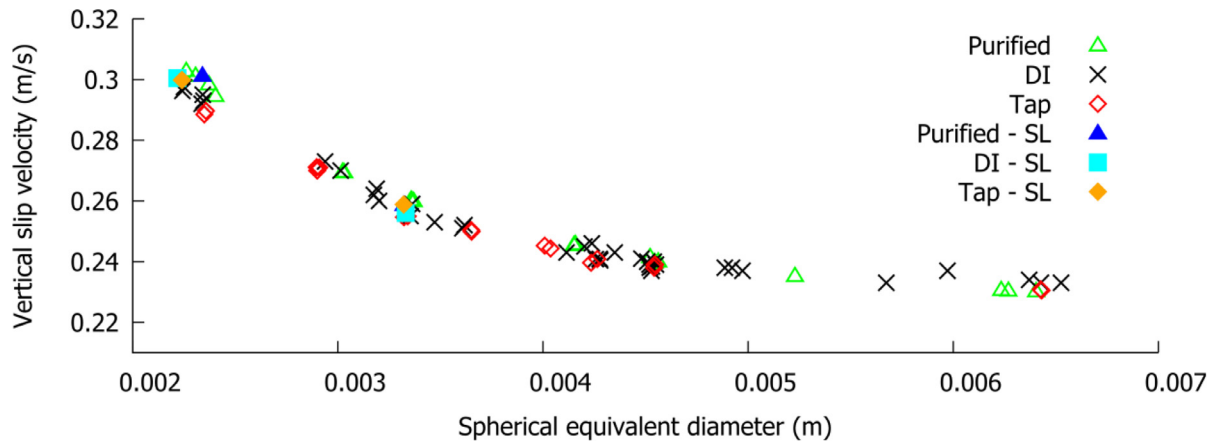


Fig. 9. Average vertical slip velocity for the different types of water and in comparison to pretests in quasi-stagnant liquid (SL).

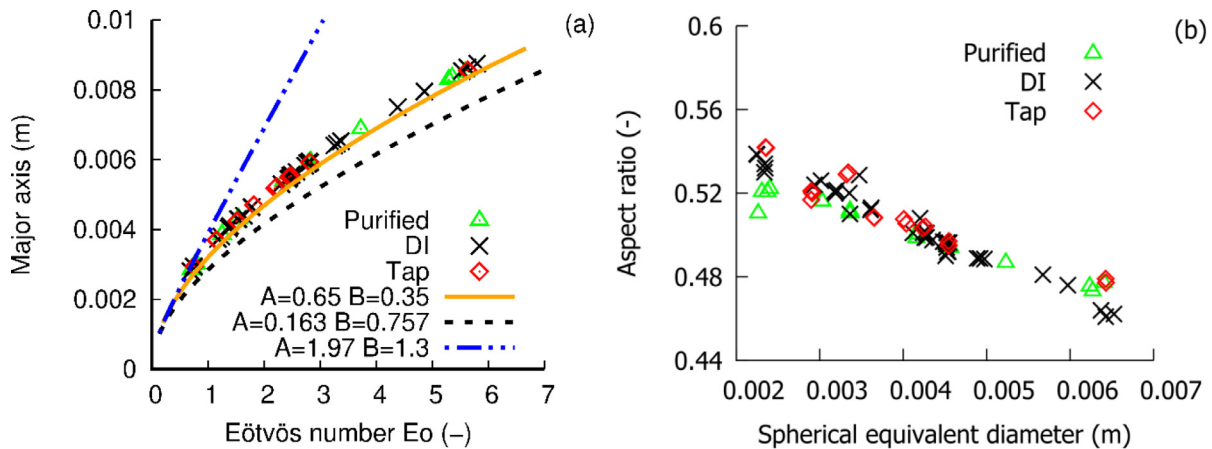


Fig. 10. Bubble shape results. (a) Average bubble major axis in comparison to correlations from the literature. A and B are coefficients for Eq (5); (b) Average aspect ratios of the different types of water.

Okawa et al., 2003 obtained their coefficients also for experimental data with $Eo < 1$.

More suitable are the coefficients $A=0.65$, $B=0.35$ for the present size range, which we obtained by fitting the experimental data of Ziegenhein and Lucas (2017). Their data was obtained with comparable water quality as in this work, which underlines that the Wellek correlation is not suitable for a clean air/water system. The rather small differences between the present results and the fit to the data of Ziegenhein and Lucas (2017) can be explained by the generality of the latter, since data from different bubble column setups were analyzed in their work.

The comparison of the aspect ratios in Fig. 10(b) reveals again a slightly more deformed bubble shape in the purified case for small bubbles. The difference is again very small and only visible due to the small axis range, which explains why the differences are not visible in the major axis plot in Fig. 10(a). With increasing bubble size no difference is present between the different types of water. Hence, also in the lift force experiments an effect of impurities on the velocity and shape could be observed only for the smallest bubble size.

4.4. Lift coefficient results

In the following, the lift coefficient results for the different types of water are shown and discussed. Fig. 11 shows the lift coefficient against the modified Eötvös number Eo_{\perp} . For all investigated water types the lift coefficient takes positive values for

smaller Eo_{\perp} and transitions to negative values with increasing Eo_{\perp} . Only a few data points are available for larger Eo_{\perp} , since the uncertainties are the highest (cf. section 4.2) and a stable generation of such larger bubbles showed some complications. While the DI-water and tap water results show no difference to each other, the purified water case shows systematic lower lift coefficient results in comparison to the two other cases independent of the bubble size. This is quite surprising, since the velocity and shape results discussed in the previous section are the same for almost all bubble sizes except the smallest bubbles. As all experimental parameters were kept the same, the cause must be nevertheless due to different impurity concentrations. It seems that the lift coefficient is even more sensitive to impurities than the velocity and the shape.

Due to the mentioned difficulties that complicate the lift force determination for ellipsoidal bubbles in a low-viscous system, the number of investigations suitable for comparison is limited. For a similar parameter range as in the present work, C_L has been determined quantitatively mostly with DNS, e.g. by Dijkhuizen et al. (2010b) and Feng and Bolotnov (2017). A corresponding comparison is depicted in Fig. 12, where the DI and tap water cases are combined as they can be considered the same. The results of the purified water case show a good agreement to the two DNS references. This proves the “cleanliness” of the bubbles in the purified case as the DNS cases do not include any effect of contamination. Moreover, it proves the validity and accuracy of the measurements and the used method.

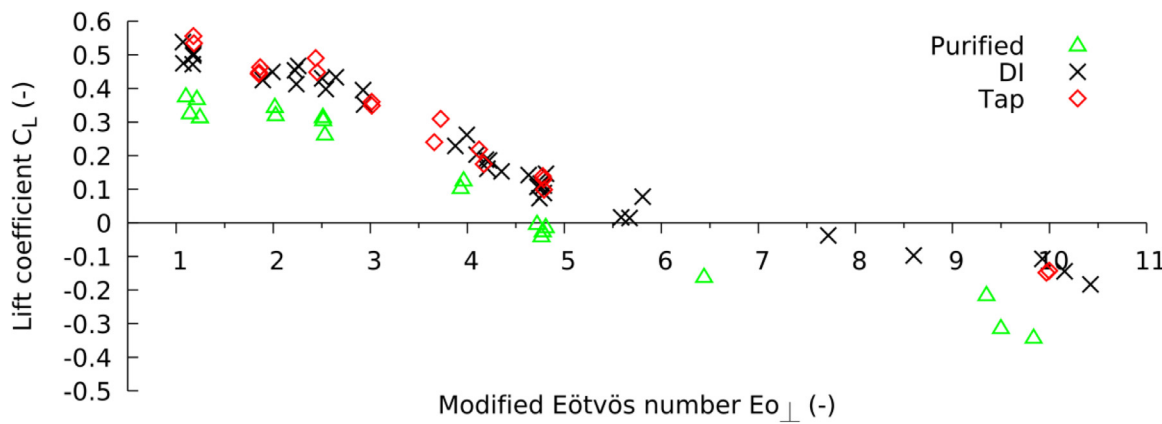


Fig. 11. Average lift coefficient results in dependence on the modified Eötvös number Eo_{\perp} for purified, DI and tap water.

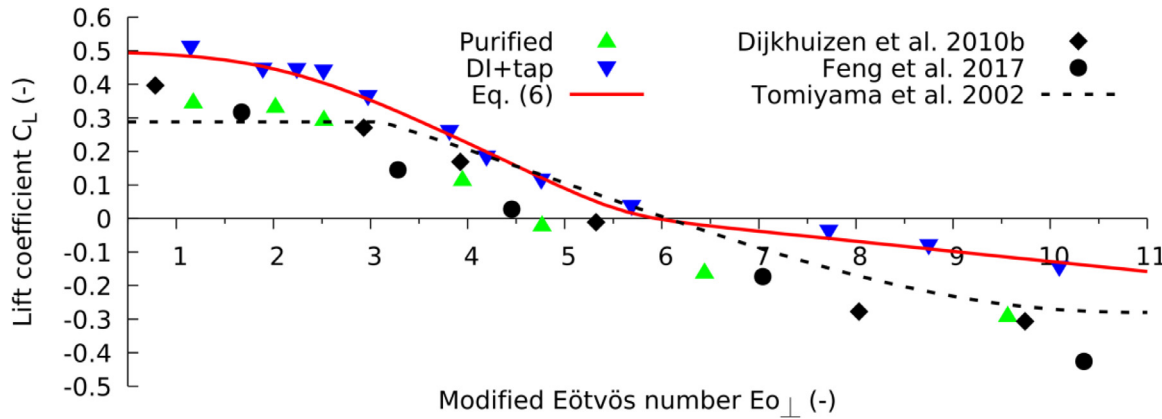


Fig. 12. Comparison of the lift coefficient results to literature data.

Although the data basis for the correlation by Tomiyama et al. (2002) was obtained in high-viscous liquids, it is very popular and often used in CFD simulations of bubbly flows even in the case of air-water flows. A good agreement of this correlation to the DI+tap water results is visible for the size range $4 < Eo_{\perp} < 6$, while for smaller and larger bubbles the agreement to the purified case is better. Both seem to be coincidental circumstances due to the mentioned dependency of C_L on the Morton number. Nevertheless, the comparison demonstrates that the Tomiyama correlation shows some deviations for both water cases in the present size range.

Although only relevant for idealized cases, the C_L of uncontaminated ellipsoidal bubbles can be calculated with the correlation proposed by Dijkhuizen et al. (2010b), which also reasonably fits the purified results of the present work. More relevant for practical cases are the results of the slightly contaminated case with DI and tap water, as the majority of corresponding applications and CFD-grade data sets will most likely show a similar amount of impurities. To account for the observed differences to the Tomiyama correlation, some modifications are required.

The correlation by Legendre and Magnaudet (1998), which depends on the dimensionless shear rate Sr and the bubble Reynolds number Re , gives a C_L value close to 0.5 for high Reynolds number bubbles. This seems to be also a reasonable choice as an initial value for the present size range, since it gives a good connection between known C_L values of spherical bubbles (Auton, 1987; Legendre and Magnaudet, 1998; Takagi and Matsumoto, 2011) and the results of the smallest bubbles in the DI and tap water case. The decreasing lift coefficient regime can be correlated by a fit to the current data as shown in Fig. 11. The combination of the

Legendre and Magnaudet (1998) correlation $f(Sr, Re)$ and the applied fit $f(Eo_{\perp})$ reads as follows:

$$C_L = f(Sr, Re) - f(Eo_{\perp}), \quad (6)$$

with

$$f(Sr, Re) = \left(\left(\frac{6}{\pi^2} \frac{1}{\sqrt{Re Sr}} \frac{2.255}{(1+0.2\epsilon^{-2})^{3/2}} \right)^2 + \left(0.5 \frac{Re+16}{Re+29} \right)^2 \right)^{1/2}, \quad (7)$$

$$Re = \frac{\rho_L u_{Slip} d_B}{\mu}; Sr = \frac{d_B \gamma}{u_{Slip}}, \quad \epsilon = \left(\frac{Sr}{Re} \right)^{1/2}, \quad (8)$$

and

$$(Eo_{\perp}) = \frac{\ln(1 + \exp(-12(G)))}{12}, \quad (9)$$

$$G = 0.11 \frac{\ln(1 + \exp(4(Eo_{\perp} - 5.6)))}{4} - 0.14(Eo_{\perp} - 5.2) - 0.44. \quad (10)$$

Since the proposed fit is again based on the modified Eötvös number Eo_{\perp} (cf. Eq. (1)), a correlation to calculate the bubble major axis from a given sphere-volume equivalent diameter is required in many cases. As discussed in section 4.3 the correlation of Wellek et al. (1966) can be used, but the coefficients have to be adjusted (Eq. (1) with coefficients $A=0.65$ and $B=0.35$) in order to better predict the bubble major axis and hence Eo_{\perp} . Further discussion on C_L of clean bubbles will be made in the near future.

5. Conclusion and discussion

The lift coefficient of single bubbles rising through a linear shear field is investigated in the present work. The bubbles are in the ellipsoidal size range with sphere-volume equivalent diameters of 2.2–6.5 mm. For determining the lift force, a recently developed method published by Ziegenhein et al. (2018) is used and upgraded to measure liquid velocities and bubble movements simultaneously. This is achieved by using a small DOF and suitable post-processing routines. The liquid phase velocity is determined with the so-called Particle Shadow Velocimetry (PSV) method and suitable processing techniques for bubbly flows, while for the bubble identification an edge-detection algorithm based on the sharpness gradient is used. This allows to analyze only bubbles in the center of the experimental setup and therefore in the same region as the determined velocity field.

In order to test the sensitivity of the lift force on impurities in terms of small amounts of surfactants, experiments were carried out with three different types of water, namely purified, DI and tap water. Beforehand, attempts were made to quantify the purification degree by determining contamination related bubble properties in quasi-stagnant liquid. While no difference in bubble velocity and shape could be revealed for bubbles larger than 3 mm, the DI and tap water case showed some small differences to the purified case for smaller bubble sizes.

The lift force experiments revealed systematically larger lift coefficient results in the DI and tap water cases in comparison to the purified water case for all bubble sizes. A comparison to literature data showed a good agreement of the purified results to comparable DNS studies, which underlines the accuracy and reliability of the method. However, the offset in the two other cases demonstrates that even such small amounts of impurities can be of importance and need to be incorporated in corresponding lift force DNS to reflect more relevant situations in practical applications.

The correlation by Tomiyama et al. (2002), which is often used in CFD simulations, fits the present data in the transition zone of decreasing lift coefficient up to the critical size quite well. To account for the differences obtained in the present work outside of this region, a new correlation to calculate C_L is presented in Eq. (6). It consists of a combination of the correlation of Legendre and Magnaudet (1998) for spherical bubbles and a fit to the current results in dependence on Eo_{\perp} for ellipsoidal bubbles. Additionally, a correlation to calculate the major axis is needed. The coefficients A=0.65 and B=0.35 seem to be more suitable to predict the bubble major axis of clean bubbles in the present size range and should be used to calculate C_L of ellipsoidal bubbles in air-water flows. It should be noted that both, the proposed lift coefficient correlation as well as the proposed shape correlation coefficients are valid only for bubble sizes smaller than 6.5 mm.

Declaration of Competing Interest

The authors declare that they have no known competing financial interests or personal relationships that could have appeared to influence the work reported in this paper.

CRediT authorship contribution statement

H. Hessenkemper: Investigation, Visualization, Validation, Software, Data curation, Writing - original draft. **T. Ziegenhein:** Methodology, Conceptualization, Software. **R. Rzebak:** Formal analysis, Writing - review & editing. **D. Lucas:** Conceptualization, Supervision, Project administration, Writing - review & editing. **A. Tomiyama:** Conceptualization, Writing - review & editing.

References

- Adoua, R., Legendre, D., Magnaudet, J., 2009. Reversal of the lift force on an oblate bubble in a weakly viscous linear shear flow. *J. Fluid Mech.* 628, 23–41.
- Aoyama, S., Hayashi, K., Hosokawa, S., Lucas, D., Tomiyama, A., 2017. Lift force acting on single bubbles in linear shear flows. *Int. J. Multiph. Flow* 96, 113–122.
- Auton, T.R., 1987. The lift force on a spherical body in a rotational flow. *J. Fluid Mech.* 183, 199–218.
- Besagni, G., Inzoli, F., 2016. Comprehensive experimental investigation of counter-current bubble column hydrodynamics: Holdup, flow regime transition, bubble size distributions and local flow properties. *Chem. Eng. Sci.* 146, 259–290.
- Bothe, D., Schmidtke, M., Warnecke, H.J., 2006. VOF-simulation of the lift force for single bubbles in a simple shear flow. *Chem. Eng. Technol.* 29, 1048–1053.
- Bröder, D., Sommerfeld, M., 2007. Planar shadow image velocimetry for the analysis of the hydrodynamics in bubbly flows. *Meas. Sci. Technol.* 18, 2513–2528.
- Calzavarini, E., Cencini, M., Lohse, D., Toschi, F., 2008. Quantifying Turbulence-Induced Segregation of Inertial Particles. *Phys. Rev. Lett.* 101, 084504.
- Cuenot, B., Magnaudet, J., Spennato, B., 1997. The effects of slightly soluble surfactants on the flow around a spherical bubble. *J. Fluid Mech.* 339, 25–53.
- Dijkhuizen, W., Roghair, I., Van Sint Annaland, M., Kuipers, J.A.M., 2010a. DNS of gas bubbles behaviour using an improved 3D front tracking model—Drag force on isolated bubbles and comparison with experiments. *Chem. Eng. Sci.* 65, 1415–1426.
- Dijkhuizen, W., van Sint Annaland, M., Kuipers, J.A.M., 2010b. Numerical and experimental investigation of the lift force on single bubbles. *Chem. Eng. Sci.* 65, 1274–1287.
- Duineveld, P.C., 1995. The Rise Velocity and Shape of Bubbles in Pure Water at High Reynolds Number. *J. Fluid Mech.* 292, 325–332.
- Ervin, E.A., Tryggvason, G., 1997. The rise of bubbles in a vertical shear flow. *J. Fluids Eng. Trans. ASME* 119, 443–449.
- Estevezordal, J., Goss, L., 2005. PIV with LED: Particle Shadow Velocimetry (PSV) Technique. 43rd AIAA Aerospace Sciences Meeting and Exhibit.
- Fan, L., Tsuchiya, K., 1990. Bubble Wake Dynamics in Liquids and Liquid-Solid Suspensions. Butterworth-Heinemann, Oxford.
- Feng, J., Bolotnov, I.A., 2017. Interfacial force study on a single bubble in laminar and turbulent flows. *Nucl. Eng. Des.* 313, 345–360.
- Hessenkemper, H., Ziegenhein, T., 2018. Particle Shadow Velocimetry (PSV) in bubbly flows. *Int. J. Multiph. Flow* 106, 268–279.
- Hessenkemper, H., Ziegenhein, T., Lucas, D., 2020. Contamination effects on the lift force of ellipsoidal air bubbles rising in saline water solutions. *Chem. Eng. J.* 386, 121589.
- Kariyasaki, A., 1987. Behaviour of a Gas Bubble in a Liquid Flow with a Linear Velocity Profile. *Trans. Japan Soc. Mech. Eng. Ser. B* 53, 744–749.
- Lamb, H., 1932. Hydrodynamics. Cambridge University Press.
- Legendre, D., Magnaudet, J., 1998. The lift force on a spherical bubble in a viscous linear shear flow. *J. Fluid Mech.* 368, 81–126.
- Lopez de Bertodano, M., Lahey, R.T., Jones, O.C., 1994. Phase distribution in bubbly two-phase flow in vertical ducts. *Int. J. Multiph. Flow* 20, 805–818.
- Lucas, D., Prasser, H.M., Manera, A., 2005. Influence of the lift force on the stability of a bubble column. *Chem. Eng. Sci.* 60, 3609–3619.
- Lucas, D., Tomiyama, A., 2011. On the role of the lateral lift force in poly-dispersed bubbly flows. *Int. J. Multiph. Flow* 37, 1178–1190.
- Muniz, M., Sommerfeld, M., 2020. On the force competition in bubble columns: A numerical study. *Int. J. Multiph. Flow*, 103256.
- Okawa, T., Tanaka, T., Kataoka, I., Mori, M., 2003. Temperature effect on single bubble rise characteristics in stagnant distilled water. *Int. J. Heat Mass Transf.* 46, 903–913.
- Parekh, J., Rzebak, R., 2018. Euler–Euler multiphase CFD-simulation with full Reynolds stress model and anisotropic bubble-induced turbulence. *Int. J. Multiph. Flow* 99, 231–245.
- Sokolichin, A., Eigenberger, G., Lapin, A., 2004. Simulation of Buoyancy Driven Bubbly Flow: Established Simplifications and Open Questions. *AIChE J* 50, 24–45.
- Tagawa, Y., Takagi, S., Matsumoto, Y., 2014. Surfactant effect on path instability of a rising bubble. *J. Fluid Mech.* 738, 124–142.
- Takagi, S., Matsumoto, Y., 2011. Surfactant Effects on Bubble Motion and Bubbly Flows. *Annu. Rev. Fluid Mech.* 43, 615–636.
- Tomiyama, A., Celata, G.P., Hosokawa, S., Yoshida, S., 2002a. Terminal velocity of single bubbles in surface tension force dominant regime. *Int. J. Multiph. Flow* 28, 1497–1519.
- Tomiyama, A., Sou, A., Zun, I., Kanami, N., Sakaguchi, T., 1995. Effects of Eötvös Number and Dimensionless Liquid Volumetric Flux on Lateral Motion of a Bubble in a Laminar Duct Flow. *Multiphase Flow* 1995.
- Tomiyama, A., Tamai, H., Zun, I., Hosokawa, S., 2002b. Transverse migration of single bubbles in simple shear flows. *Chem. Eng. Sci.* 57, 1849–1858.
- Veldhuis, C., Biesheuvel, A., Van Wijngaarden, L., 2008. Shape oscillations on bubbles rising in clean and in tap water. *Phys. Fluids* 20, 040705.
- Wellek, R.M., Agrawal, A.K., Skelland, A.H.P., 1966. Shape of liquid drops moving in liquid media. *AIChE J* 12, 854–862.
- Ziegenhein, T., Garcon, M., Lucas, D., 2016. Particle tracking using micro bubbles in bubbly flows. *Chem. Eng. Sci.* 153, 155–164.
- Ziegenhein, T., Lucas, D., 2017. Observations on bubble shapes in bubble columns under different flow conditions. *Exp. Therm. Fluid Sci.* 85, 248–256.
- Ziegenhein, T., Tomiyama, A., Lucas, D., 2018. A new measuring concept to determine the lift force for distorted bubbles in low Morton number system: Results for air/water. *Int. J. Multiph. Flow* 108, 11–24.
- Zun, I., 1980. The transverse migration of bubbles influenced by walls in vertical bubbly flow. *Int. J. Multiph. Flow* 6, 583–588.